Supporting Information

Limmer and Chandler 10.1073/pnas.1407277111

SI Text

Glass Transition Temperatures and Nonequilibrium Lengths. This section summarizes formulas we use in this paper to predict glass transition temperatures. The formulas are derived in refs. 1, 2.

Heterogeneous dynamics below the onset is characterized by the concentration c of localized soft spots or excitations. At equilibrium, $c\sigma^3 = \exp(-\tilde{\beta})$, where $\tilde{\beta} = [1/T - 1/T_o(p)]\, J_\sigma(p) > 0$ and $J_\sigma(p)$ is the free energy or reversible work to move a molecule a molecular diameter σ. The pressure dependence of $J_\sigma(p)$ and $T_o(p)$ is important when considering the behavior of water.

Whereas dynamics above the onset temperature is unstructured, like random motion in a mean field, dynamics below the onset temperature is controlled by excitations facilitating the birth and death of neighboring excitations. At equilibrium, the mean-free path between excitations is

$$\ell(T) = \sigma \exp\left(\tilde{\beta}/d_f\right), \qquad \text{[S1]}$$

where d_f is the fractal dimensionality of the path. For three-dimensional structural glass, $d_f \approx 2.4(3)$.

Collective reorganization is required to move a molecule to a new enduring position, so that its reorganization energy depends upon the length of that displacement. Specifically, $J_{\sigma'} = J_\sigma[1 + \gamma \ln(\sigma'/\sigma)]$. This logarithmic growth of energy with length is universal, but the constants J_σ and γ are system dependent (3, 4). As a result of the logarithmic growth, the structural relaxation time τ is

$$\tau(T) = \tau_{MF} \exp\left\{\tilde{\beta}\, \gamma \ln[\, \ell(T)/\sigma]\right\}, \quad T < T_o(p), \qquad \text{[S2]}$$

where τ_{MF} is τ for $T \geq T_o(p)$. In general, τ_{MF} is a weak function of T and p, but we neglect that dependence in comparison with the much larger temperature variation of the right-hand side of Eq. **S2**. At equilibrium, Eqs. **S1** and **S2** combine to give the familiar super-Arrhenius parabolic law.

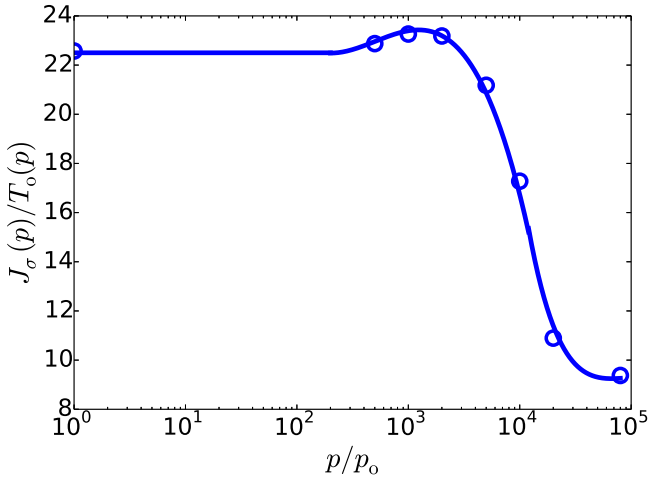

Fig. S1. Reduced energy scale $J_\sigma(p)/T_o(p)$ as a function of pressure. Circles are results computed with the mW model following methods detailed in refs. 1 and 2. Corresponding states analysis (3) indicates that these results should hold for all reasonable models of water as well as for the actual substance. The solid line is the spline fit to the data.

Super-Arrhenius relaxation is associated with underlying hierarchical dynamics, where relaxation depends upon the size of relaxing domains. This dependence is responsible for a glass transition when the material is cooled at a rate ν. Specifically, the system transitions from ergodic to nonergodic behavior at a temperature T_g, where

$$1/\nu = |d\tau/dT|_{T_g}, \qquad \text{[S3]}$$

below which $\ell(T)$ is locked at its nonequilibrium value $\ell_{ne} = \ell(T_g)$. Therefore

$$1 = \frac{2\, \nu\, \tau_{MF}\, \tilde{\beta}_g \gamma\, J_\sigma}{d_f\, T_g^2} \exp\left(\tilde{\beta}_g^2 \gamma \Big/ d_f\right), \qquad \text{[S4]}$$

where

$$\tilde{\beta}_g = J_\sigma(p)\left[1/T_g(p) - 1/T_o(p)\right] = d_f \ln(\ell_{ne}/\sigma), \qquad \text{[S5]}$$

or

$$\frac{1}{T_g(p)} = \frac{1}{T_o(p)} + \frac{d_f}{J_\sigma(p)} \ln(\ell_{ne}/\sigma). \qquad \text{[S6]}$$

Eq. **S6** gives the dashed lines in Fig. 1*A*.

An approximate solution to the transcendental Eq. **S4** is useful when T_o and T_g are of the same order and $\tilde{\beta}_g^2\gamma/d_f \gg \ln(\tilde{\beta}_g\gamma/d_f)$. In that case

$$\ln(\ell_{ne}/\sigma) \approx \sqrt{-\ln\left[2\, \nu\, \tau_{MF}\, \gamma\, J_\sigma(p)/T_o^2(p)\right]/d_f\, \gamma}. \qquad \text{[S7]}$$

This solution can serve as the first guess to the numerical solution, the first guess differing from the numerical solution for water by a few percent.

Because $\ell(T) = \ell_{ne}$ for all $T < T_g$, the relaxation time τ, Eq. **S2**, is Arrhenius for that regime. If the glass with its fixed ℓ_{ne} is cooled to a very low temperature, and then warmed on a time scale of t_w, it will undergo a transition at an apparent glass transition temperature T_{ag}, where $t_w = \tau_{MF} \exp\{\tilde{\beta}_{ag}\, \gamma \ln(\ell_{ne}/\sigma)\}$. Accordingly,

$$\frac{1}{T_{ag}(p)} = \frac{1}{T_o(p)} + \frac{\ln(t_w/\tau_{MF})}{\gamma\, J_\sigma(p) \ln(\ell_{ne}/\sigma)}\ . \qquad \text{[S8]}$$

Eq. **S8** yields the dotted lines in Fig. 1*A*, with $T_{ag}(p)$ evaluated for a warming-time scale of minutes, i.e., $t_w \approx 10^2\ \text{s} \approx 10^{14}\ \tau_{MF}$.

Application of these formulas requires $T_o(p)$, $J_\sigma(p)$, and τ_{MF}. The low-pressure forms have been determined previously (5). High-pressure behaviors have been determined similarly. Fig. 1*A* shows the behavior of $T_o(p)$, and its form is well approximated by a spline,

$$\begin{aligned} T_o(p)/T_o &= -0.015 \log(p/p_o) + 0.976, \quad 0 < p/p_o < 5\times 10^2 \\ &= 0.199\, \log^2(p/p_o) - 1.344 \log(p/p_o), \\ &\quad + 3.118, \quad 5\times 10^2 < p/p_o < 2\times 10^3 \\ &= 0.173\left(\log^2(p/p_o) - 1.078 \log(p/p_o)\right) \\ &\quad + 2.521, \quad 2\times 10^3 < p/p_o < 8\times 10^4. \end{aligned} \qquad \text{[S9]}$$

Table S1. Nonequilibrium length, time, and energy scales for LDA ice at ambient pressure

ℓ_{ne}/nm	ν/K s^{-1}	τ_g/s	T_g/T_o	T_{ag}/T_o
1.5	10^8	10^{-9}	0.80	0.48
5.0	10^4	10^{-4}	0.73	0.55
10.0	0.1	10^2	0.65	0.65

Fig. S1 shows the behavior of $J_\sigma(p)/T_o(p)$, and its form is well approximated by a spline,

$$\begin{aligned} J_\sigma(p)/T_o(p) &= 22.5, \quad 0 < p/p_o < 2\times 10^2 \\ &= -3.9(\log(p/p_o) - 2.7)^3 + 1.8\log(p/p_o), \\ &\quad + 18.1, \quad 2\times 10^2 < p/p_o < 1.2\times 10^4 \\ &= 6.0(\log(p/p_o) - 5.1)^4 + 0.5\log(p/p_o) \\ &\quad + 6.8, \quad 1.2\times 10^4 < p/p_o < 8\times 10^4. \end{aligned} \qquad \textbf{[S10]}$$

Table S1 illustrates predictions of these formulas applied to water at ambient conditions, computing T_{ag} with the warming-time scale of minutes, i.e., $t_w = 10^2$ s.

Dynamics of Transformations of Amorphous Ices. In this section we provide a few more examples of dynamics that follow from our simulated high-density amorphous (HDA) and low-density amorphous (LDA) phases.

The first example focuses on the reversibility of pressurizing and depressurizing the amorphous ices to transition between HDA and LDA. The nature of these processes is illustrated in Fig. S2. Specifically, configurations taken from the HDA basin prepared with large s are first quenched to lower temperature and to $s = 0$. Then the configuration and volume are evolved with Nosé–Hoover (6) equations of motion with a constant rate of change of the pressure and its reverse. Over 1,000 trajectories generated in this way are used to compute the time-dependent density depicted in Fig. S2. The ability to reverse the HDA to LDA transition demonstrates that the materials produced by the s ensemble are robust solids.

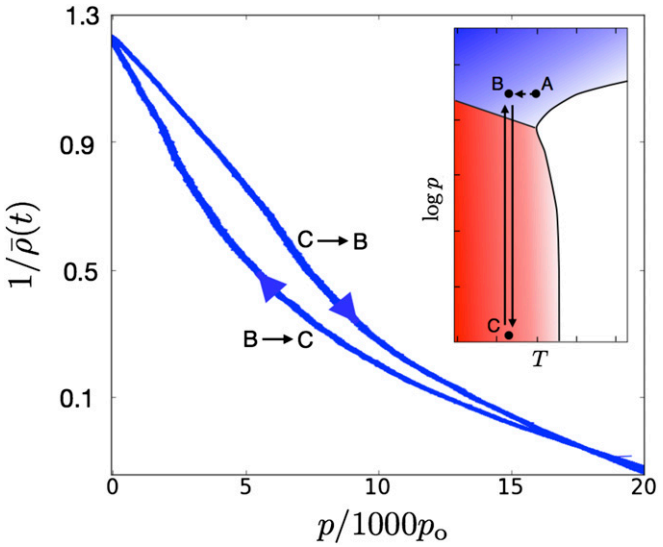

Fig. S2. Forward and backward transitions between HDA and LDA. Configurations taken from HDA prepared at $s > s^*$, $T/T_o = 0.8$, and $p/p_o = 20\times 10^3$, state A, are instantly quenched at constant pressure to a temperature $T/T_o = 0.6$, state B, where it is annealed with $s = 0$ for 2000 Δt. Then the pressure is changed at constant temperature at a rate of –5 kbar/ns to $p/p_o = 1$, state C. The pressure is then changed at constant temperature with a rate of 5 kbar/ns, back to state B. (*Inset*) Illustration of the paths. The time dependence of the averaged reduced density or volume is illustrated in the main graph.

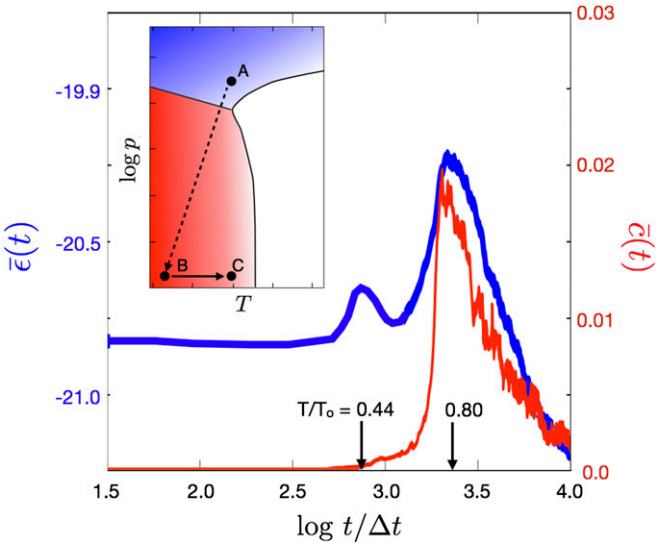

Fig. S3. Time dependence of the potential energy and number of enduring displacements of HDA heated at low pressure. Configurations taken from HDA prepared at $s > s^*$, $T/T_o = 0.8$, and $p/p_o = 20\times 10^3$, state A, are instantly quenched to $s = 0$, $T/T_o = 0.32$, and $p/p_o = 1$, state B. The temperature is then changed at constant pressure at a rate of 10 K/ns to $T/T_o = 0.8$, state C. Configurations are then annealed at this temperature for $t/\Delta t = 7.5\times 10^3$. (*Inset*) Illustration of this path The time dependence of the averaged potential energy per particle, $\bar{\epsilon}(t)$ in units of T_o, and the excitation concentration $\bar{c}(t)$ are shown in the main graph. The black arrows indicate the temperature reached at two particular points in time.

The second example considers the time dependence of the potential energy per particle $\bar{\epsilon}(t)$ and the number of EDs per particle $\bar{c}(t)$ of very cold HDA brought to a low pressure where it is then warmed. From our discussion of phenomenology in the main text and from experimental work (7), we expect this protocol to produce two calorimetric peaks—one apparent glass transition where HDA transforms to LDA, and another apparent glass transition where LDA melts into a nonequilibrium liquid from which crystal ice coarsens.

We observe this behavior, as illustrated in Fig. S3, and the temperatures at which the transitions occur can be understood in terms of the equations presented in the previous section. The figure shows the results obtained from averaging 1,000 independent trajectories initiated from the HDA configurations, with a warming-time scale $t_w \approx 10^3 \tau_{MF}$. Eq. **S8** then predicts a transition at $T_{ag} \approx 0.44\ T_o$, in good agreement where the low-temperature transition is detected in the trajectories. Above that temperature, the radial distribution functions found from our simulation indicate that the resulting amorphous solid is the LDA material. In that case, the activation energy (or equivalently, the value of J_σ) has changed from that locked in from the higher-pressure HDA material to that of the LDA material. Eq. **S8** then gives $T_{ag} \approx 0.80$ for the temperature that LDA will melt, again in good agreement with the results of our trajectories.

Having gained confidence in our theoretical analysis through comparison with simulation, we now turn to the experimental observations of two-step relaxation (7). These recent experiments have found that a stabilized version of HDA brought to low temperatures and pressures exhibits a calorimetric peak at $T \approx 130$ K. By taking this value for T_{ag} and applying Eq. **S8** with $t_w = 100$ s, we conclude that $\ell_{ne} \approx 5$ nm for this version of HDA. The corresponding T_{ag} for LDA can then be predicted using this

value for ℓ_{ne} together with the low-pressure LDA value for J_σ. This evaluation predicts $T_{ag} \approx 150$ K for the LDA material that is produced by melting the stabilized HDA. This predicted position for a second calorimetric peak is in harmony with experiment (7).

Notice that, had experimentalists not stabilized the HDA through annealing, the data shown in Fig. 1*A* suggest that the HDA material would have $\ell_{ne} \approx 1.5$ nm. In that case, T_{ag} computed from Eq. **S8** for that HDA material would be ≈ 85 K. Such a low value for the temperature at which the low pressure form of HDA would become unstable indicates why two-step melting was not detected without first annealing to create a more stable HDA.

Based upon indirect evidence, experimentalists have interpreted two-step melting of amorphous ices as indicative of two distinct liquid phases (7, 8). We find nothing in our simulations to support the idea. The time dependence of the excitation concentration $\overline{c}(t)$ shows that the material remains solid-like until reaching the apparent glass transition temperature of LDA, which with the warming rate of our simulations occurs near $0.8\ T_o$. In other words, some reorganization does occur to allow the transition from HDA to LDA, but the low mobility of a glass remains until ergodic states are accessed at the apparent glass transition temperature for LDA.

1. Keys AS, Garrahan JP, Chandler D (2013) Calorimetric glass transition explained by hierarchical dynamic facilitation. *Proc Natl Acad Sci USA* 110:4482–4487.
2. Limmer DT (2013) The length and time scales of water's glass transitions. arXiv: 1312.2609.
3. Keys AS, Hedges LO, Garrahan JP, Glotzer SC, Chandler D (2011) Excitations are localized and relaxation is hierarchical in glass-forming liquids. *Phys Rev X* 1:021013.
4. Elmatad YS, Chandler D, Garrahan JP (2009) Corresponding states of structural glass formers. *J Phys Chem B* 113(16):5563–5567.
5. Limmer DT, Chandler D (2012) Phase diagram of supercooled water confined to hydrophilic nanopores. *J Chem Phys* 137(4):044509.
6. Martyna GJ, Klein ML, Tuckerman M (1992) Nosé–Hoover chains: The canonical ensemble via continuous dynamics. *J Chem Phys* 97:2635–2643.
7. Amann-Winkel K, et al. (2013) Water's second glass transition. *Proc Natl Acad Sci USA* 110:17720–17725.
8. Amann-Winkel K, et al. (2012) Limits of metastability in amorphous ices: The neutron scattering Debye-Waller factor. *Phys Chem Chem Phys* 14(47):16386–16391.